MARS GLOBAL SURVEYOR OBSERVATIONS OF SOLAR WIND MAGNETIC FIELD DRAPING AROUND MARS

DANA H. CRIDER[1], DAVID A.BRAIN[2], MARIO H. ACUÑA[3], DIDIER VIGNES[3], CHRISTIAN MAZELLE[4] and CESAR BERTUCCI[4]

[1]*Catholic University of America, Dept. of Physics., Washington, DC, U.S.A.*
[2]*University of Colorado, Boulder, CO, U.S.A.*
[3]*Code 695, NASA Goddard Space Flight Center, Greenbelt, MD, U.S.A.*
[4]*Centre d'Etude Spatiale des Rayonnements - CNRS/UPS, Toulouse, France*

Abstract. We examine the magnetic field in the martian magnetosheath due to solar wind draping. Mars Global Surveyor provided 3-D vector magnetic field measurements at a large range of altitudes, local times, and solar zenith angles as the spacecraft orbit evolved. We choose orbits with very clean signatures of draping to establish the nominal morphology of the magnetic field lines at local times of near-subsolar and near-terminator. Next, using a compilation of data from Mars Global Surveyor, we determine the average magnetic field morphology in the martian magnetosheath due to the solar wind interaction. The topology of the field is as expected from previous observations and predictions. The magnetic field magnitude peaks at low altitude and noon magnetic local time and decreases away from that point. The magnetic field has an inclination from the local horizontal of 5.6° on average in the dayside magnetosheath and 12.5° on the nightside. The inclination angle is closest to zero at noon magnetic local time and low altitude. It increases both upward and to later local times. The magnetic field in the induced magnetotail flares out from the Mars–Sun direction by 21°. Finally, we compare the observations to gasdynamic model predictions and find that the shocked solar wind flow in the martian magnetosheath can be treated as a gasdynamic flow with the magnetic pileup boundary as the inner boundary to the flow.

1. Introduction

Although it was known from previous missions to Mars that Mars had at most a weak planetary magnetic field (Dolginov *et al.*, 1973; Dolginov, 1978), the arrival of Mars Global Surveyor (MGS) established Mars as primarily an ionospheric obstacle to the solar wind (SW) flow (Acuña *et al.*, 1998). Crustal magnetic fields contribute to the overall obstacle; however, their effects appear to be highly localized (Mitchell *et al.*, 2001; Crider *et al.*, 2002). Therefore, both on average and in regions away from the strong crustal features, the SW interaction with Mars has common elements with Venus (Cloutier *et al.*, 1999) and with comets (Mazelle *et al.*, 2002).

In such an interaction, the conducting ionosphere and mass loading limits act as the obstacle to the SW flow (Alfvén, 1957). The impinging interplanetary magnetic field (IMF) can not completely penetrate the conducting ionosphere. The
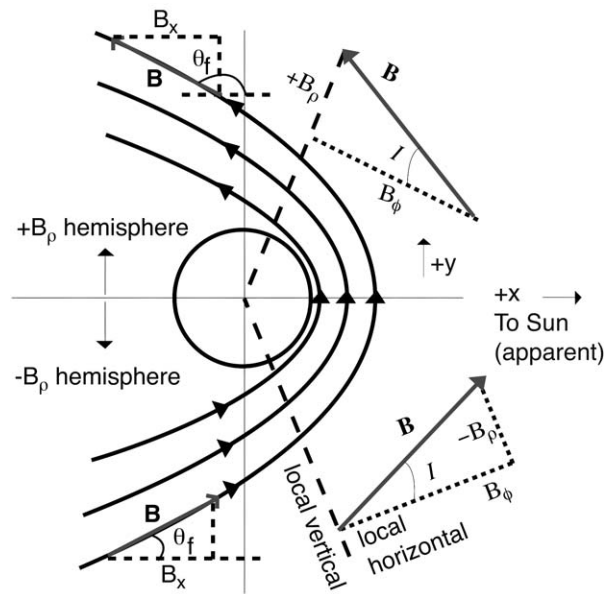
Figure 1. Cartoon depicting the geometry of magnetic field lines in the 'draping' regime. The coordinate system and angles are defined in Sections 2 and 4.

IMF 'hangs' in front of the planet. The result is that an induced magnetosphere is created that consists of magnetic field lines from the SW that are 'draped' around the obstacle (see Figure 1). The region immediately downstream of the bow shock is typically called the 'magnetosheath'. Behind the planet, the elongated, two-lobed magnetic feature is termed the 'magnetotail'. It is similar to the Earth's magnetotail except that this tail contains IMF flux tubes instead of planetary flux tubes.

The instantaneous, global morphology of the magnetic field in a draping configuration can not be measured with only one or even a few spacecraft. However, much work has been done to create models of the interaction that accurately describe the observed magnetic field topology (Spreiter and Stahara, 1980; Tanaka, 1993; Brecht, 1997; Kallio and Koskinen, 2000; Liu *et al.*, 2001). In this paper, two approaches are taken to present data that can be used to validate those models (Russell *et al.*, 1984; Slavin *et al.*, 1983). First, one can compare the model predictions to *selected data* that are representative of typical conditions to see if the model reproduces the observations. We present such comparisons in Section 3. Alternatively, one can compare the model predictions to a *compilation of data*. By compiling data from many orbital passes that occurred under different upstream conditions, one finds the average configuration of the magnetic field, and certain diagnostic parameters can be developed for comparison with models. For that purpose, we compile a global picture of the magnetic field in the SW interaction with Mars in this work using data from the MGS Magnetometer (MAG) instrument. We limit our study to the data from the martian magnetosheath and induced magnetotail,

where crustal magnetic fields should only have minimal contributions. The results from this analysis are presented in Section 4.

2. Data Analysis

Mars Global Surveyor is not currently located in the magnetosheath; however, it did traverse that area earlier in its mission. Its first 1200 orbits were elliptical orbits that sampled altitudes from 100 km to well beyond the bow shock. Meanwhile the spacecraft trajectory was shaved down from the highly eccentric insertion orbit to the near-circular mapping orbit. MGS MAG data from the magnetosheath is available for the time period of September 13, 1997 to February 4, 1999, which we term the 'elliptical orbits'. Throughout the elliptical orbits, the spacecraft orbit was highly inclined (near-polar). Orbital parameters such as local time of orbit, latitude of periapsis, and altitude of apoapsis varied slowly. Throughout the entire elliptical orbit epoch, the spacecraft sampled a large span of altitudes and local times in the region of interest for the solar wind interaction with Mars. See Brain *et al.* (2003) and Albee *et al.* (2001) for more detailed accounts of MGS orbital coverage.

For the purpose of producing a picture of the magnetic field topology around Mars resulting from the draping of the IMF, one must ensure that the data compiled are self-compatible. Because the magnetic field in the magnetosheath is comprised of IMF lines and the direction of the upstream IMF changes with time, it is logical to align the data to a consistent upstream IMF direction. Therefore, we rotate the data on an orbit by orbit basis into a coordinate system defined by the upstream IMF direction as described below.

Data from MGS are converted to a coordinate system in which the $+x$ axis points from the center of Mars to the apparent origin of the SW. The SW appears to come from a direction of $\sim 3.5°$ off of the Mars–Sun line because of the orbital velocity of Mars around the Sun. After fixing the $\hat{x}$ direction, the $\hat{y}$ direction is determined based on the upstream IMF direction. We rotate the coordinate system around the x-axis such that the average upstream IMF lies in the $x - y$ plane and such that the y component of the magnetic field is positive. Mathematically:

$$\mathbf{B}_{SW} = \langle B_{\mathrm{IMF}x}\rangle\,\hat{\mathbf{x}} + \sqrt{\langle\mathbf{B}_{\mathrm{IMF}}\rangle^2 - \langle B_{\mathrm{IMF}x}\rangle^2}\,\hat{\mathbf{y}} + 0\hat{\mathbf{z}}, \tag{1}$$

where $\mathbf{B}_{SW}$ is the vector average upstream magnetic field in IMF-related coordinates. We refer to this coordinate system as 'IMF coordinates' or 'magnetic coordinates' interchangeably throughout this paper. This method does not account for differences in the Parker Spiral angle of the IMF.

MGS data are transformed orbit by orbit into magnetic coordinates to account for variations in IMF direction. However, the IMF also varies in magnitude. Larger IMF strengths lead to higher magnetic fields in the magnetosheath which artificially weights the data from strong IMF orbits higher in determining the average magnetic field configuration. Therefore we normalize all magnetic field values on

an orbital pass by the magnitude of the average upstream IMF for that pass. In effect, we are assuming that the magnetic field magnitude throughout the interaction region scales with the upstream value as it would if the magnetic field were completely frozen to the plasma and convected along with the flow. This is not strictly accurate; but it is preferred to the uneven weighting scenario.

Naturally, there are limits to the accuracy of the transformation in Equation (1). There is no guarantee that the IMF is constant during a periapsis pass. In fact the IMF certainly changes during some orbits as a sector boundary is crossed, for example. However, we can only determine the upstream IMF direction when there is a spacecraft there to detect it. Therefore, we are limited to determining the IMF orientation at some point along the orbit and assuming that it remains constant throughout the orbit. We recognize that, on some orbits, this is inappropriate. By compiling data from many orbits, these errors will approach the value of the intrinsic variability of IMF direction (Ness et al., 1971; Burlaga and King, 1979).

Note that there is another difficulty in determining the upstream IMF direction. The magnetometers on MGS measure the ambient magnetic field at their positions at the end of the solar array panels of the spacecraft. The magnetic field at that point is a composite of the IMF and magnetic fields originated by the spacecraft. The data we use have been calibrated to remove the contribution to the magnetic field from the spacecraft, however, some $\sim$ 1 nT contribution still exists. The IMF has a median magnitude of 4 nT during the elliptical orbit phase. This was determined by assigning an upstream IMF for each orbit then taking the median. Brain et al. (2003) have determined the median IMF at Mars by taking all of the vectors obtained well upstream of the bow shock and find an IMF of 2.5–3.0 nT. In any case, because the magnitude of the field we are trying to characterize is small, the vector components are also necessarily small. Then, an error of ± 1 nT in the magnetic field components can contribute to a large error in the derived direction of the IMF. For this reason, determining the direction of the IMF using the measurements upstream of the bow shock is problematic.

However, across the bow shock, the IMF strength is magnified. One can determine the direction of the upstream IMF by looking at the magnetic field in the $y - z$ plane just across the bow shock where the magnitude is much larger, thus lessening the relative contribution of the spacecraft field. According to the Rankine–Huginot shock jump relations, the direction of the magnetic field changes across the bow shock in that there is an amplification of the component of the magnetic field perpendicular to the shock normal and there is no change in the component of the magnetic field parallel to the shock normal. In the coordinate system with $B_z = 0$ upstream of the bow shock, $B_z = 0$ downstream of the bow shock also. However, the turbulence of the magnetic field is magnified inside the bow shock as well as the magnetic field magnitude. In order to rely on the directions determined by this method, we averaged the magnetic field vectors over 100 points starting 25 points downstream of the bow shock crossing. This corresponds to many wave cycles for most orbits and, therefore, mitigates the effects of turbulence. In this way, we

use the magnetic field measured just inside of the bow shock to determine the upstream IMF direction for each orbit. In the following sections, the accuracy of this technique will be made evident.

In summary, to convert the MGS data from Mars-Solar-Ecliptic (MSE) ($'$) coordinates to IMF (unprimed) coordinates, we perform the following transformation:

$$
\begin{bmatrix} B_x \\ B_y \\ B_z \end{bmatrix} = \frac{1}{|\mathbf{B}_{SW}|} \begin{bmatrix} 1 & 0 & 0 \\ 0 & \cos\delta & \sin\delta \\ 0 & -\sin\delta & \cos\delta \end{bmatrix} \begin{bmatrix} \cos\theta_a & \sin\theta_a & 0 \\ -\sin\theta_a & \cos\theta_a & 0 \\ 0 & 0 & 1 \end{bmatrix} \begin{bmatrix} B'_{x\mathrm{MSE}} \\ B'_{y\mathrm{MSE}} \\ B'_{z\mathrm{MSE}} \end{bmatrix}. \quad (2)
$$

where $|\mathbf{B}_{SW}|$ is the upstream IMF magnitude for the orbit, the angle that rotates the $y' - z'$ component of the upstream IMF into the $+y$ direction is $\delta \equiv \arctan(B'_{zSW}/B'_{ySW})$, and θ_a is the 3.5° aberration of the apparent SW direction.

The MGS orbit is a near-polar orbit in MSE coordinates. With the slow evolution of the local time of the orbit coupled with the slow evolution of the line of apsides, MGS's sampling of low altitude space is limited in MSE coordinates to primarily one $y - z$ quadrant (see Figure 2). As a sector boundary passes, the sign of the IMF reverses. This results in an $\sim 180°$ rotation of IMF coordinates, which provides points in the opposite hemisphere. Further, the orbit departs from a polar geometry in the IMF coordinate system inasmuch as the IMF deviates from the ecliptic plane. For the 746 orbits for which we are able to determine the upstream IMF direction, 50% are within 32° of the ecliptic plane. The other half provide most of the spatial distribution of points in IMF coordinates. Without the changing IMF direction, there would be little sampling of alternate $y - z$ quadrants by MGS.

In the draping geometry, the symmetry outlined in Table I is expected. The behavior of the magnetic field x and y components is evident from inspection of Figure 1. Figure 2 displays the draping of magnetic field lines projected in the $y - z$ plane. The z component behavior comes from the fact that the draped magnetic field line that approaches the nose of the planet at the equator must go over the pole to get past the obstacle. The part of the field line that encounters the planet will be displaced in z more than the part of the field line far away from the planet that does not encounter the obstacle. Therefore, the B_z component describes the direction of the small deviation in z for the field line to slip over or under the obstacle.

3. Data from Representative MGS Orbits

We select 2 MGS orbits (P132 and P541) to demonstrate the nominal magnetic field configuration in the martian magnetosheath at various local times (LT). These orbits, from days February 15 and September 8 of 1998, are shown in Figures 3 and 4, respectively. The local times in MSE coordinates of these orbits are from
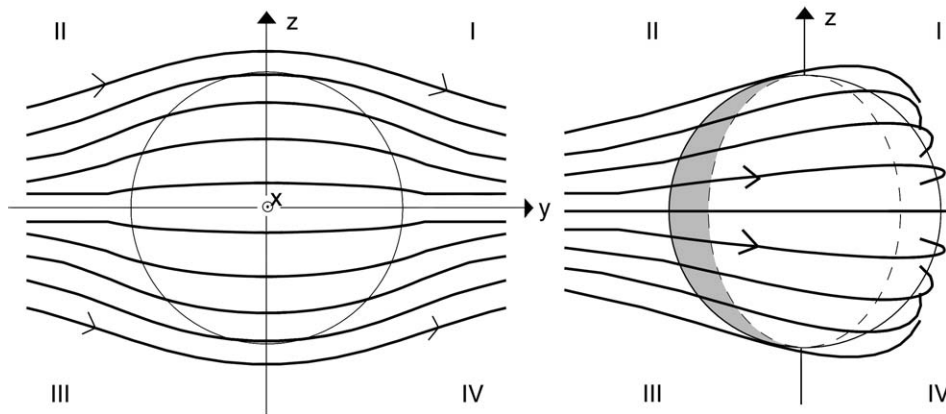
Figure 2. Cartoon depicting the geometry of magnetic field lines in the 'draping' regime. The field lines are shown in the $y - z$ plane on the left and rotated $45°$ around the z-axis on the right.

TABLE I

Expected draping magnetic field signs by $y - z$ quadrant

Quadrant	B_x	B_y	B_z
I	−	+	−
II	+	+	+
III	+	+	−
IV	−	+	+

noon and the terminator, respectively. Each figure displays the polar projection of MGS vector magnetic field measurements in IMF coordinates on the left-hand side. The right-hand panels in Figures 3 and 4 give the predicted values from the Spreiter and Stahara (1980, 1992) model for Mars under nominal conditions at the same points as given on the left. The Spreiter and Stahara model treats the SW flow as a gasdynamic (GD) flow with convected magnetic field. Although there are more sophisticated models of the interaction (e.g., Brecht, 1997; Liu *et al.*, 2001), the simplified GD representation of the interaction is very good on average, as is evident by comparing the right-hand panels to the left-hand panels.

MGS orbit P132 provides a rare glimpse of the magnetic field near the subsolar point. Figure 3 shows the projection of the magnetic field in the (x, y) plane from P132, revealing two important features of magnetic draping. First, at the nose of the planet, the magnetic field vectors have large magnitude and point in the $+y$ direction. The sign is as expected for IMF coordinates. The large magnitude stems from the pileup of field lines in front of the planet. Vectors are locally horizontal at

Magnetic Field Vectors, P132

(a) MGS Measurements (b) Spreiter Stahara Predictions
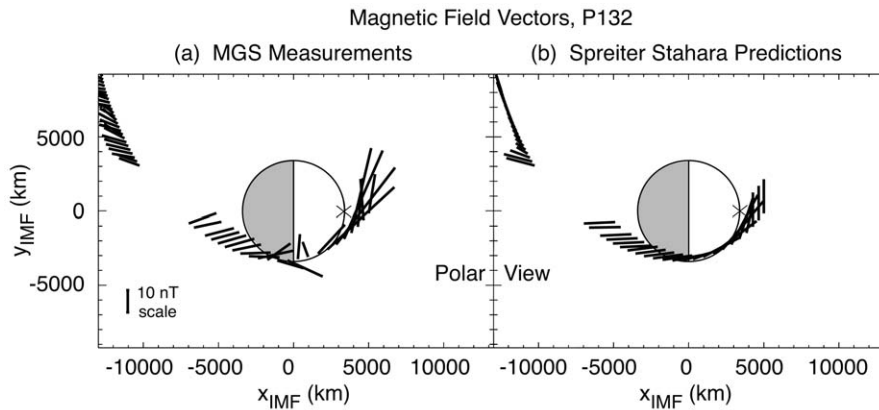
Figure 3. The $x - y$ plane projection of magnetic field vectors from MGS orbit p132 is shown. (a) is the polar view of the magnetic field vectors measured along the MGS orbital track. (b) is the predicted magnetic field by the GD model for the same points. The 'X' marks the subsolar point on the planet. The local time of the orbit was near noon, but transformation to IMF coordinates rotates the polar orbit to an orbit at 45° inclination. Periapsis occurred just sunward of the terminator.

the nose. As the trajectory moves away from the nose of the planet, an x component to the magnetic field enters as is necessary to maintain locally horizontal magnetic field (see Bertucci *et al.*, 2003). Secondly, in the tail, there are two obvious lobes to the tail. Although a data gap exists here, the two tail lobes are probably separated by the $y = 0$ plane. The vectors in the $-y$ hemisphere point sunward and the vectors in the $+y$ hemisphere point tailward.

Figure 4 shows the symmetry about the $y = 0$ plane of the magnetic field vectors. The draping of magnetic field is obvious in orbit P541 as B_x goes from tailward in the $+y$ hemisphere to a dawn-dusk orientation at $y = 0$ to sunward in the $-y$ hemisphere. Because periapsis occurred close to the equator in IMF coordinates, the inbound and outbound passes trace almost on top of one another in Figure 4. The symmetry between the $+z/-z$ hemispheres becomes clear in this view.

Direct comparison with GD model predictions suggest that the GD model does a good job of predicting the morphology of the magnetic field on representative orbits, especially when the data comes from an orbit with steady upstream conditions. For most orbits, the GD model does best when the inner boundary of the model is mapped to the Magnetic Pileup Boundary (MPB) in the data. When the inner boundary is placed elsewhere, e.g., at the ionopause, the GD model does not reproduce the observed increase of magnetic field at the MPB. Even so, the actual situation is far more complicated than indicated by the simple GD model. MGS consistently detects the IMF permeating to much lower altitudes (see Acuña *et al.*, 1998) indicating that the MPB is not the actual obstacle. Therefore, the interaction is probably better described by more sophisticated models. However, we continue
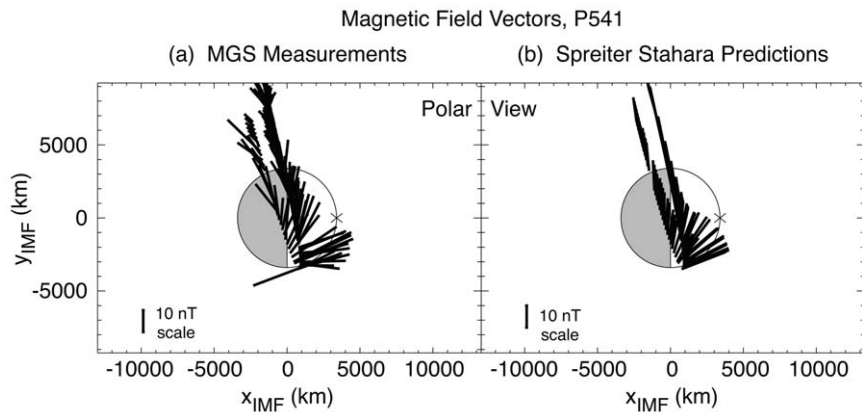
Magnetic Field Vectors, P541

(a) MGS Measurements   (b) Spreiter Stahara Predictions

Figure 4. The projection of magnetic field vectors from MGS orbit p541 into the $x-y$ plane is shown in the same format as Figure 3. The local time of the orbit was near the terminator.

to compare the data to the GD model because of its simplicity and its success in the magnetosheath.

These selected MGS orbits depict the nominal form of magnetic field draping at Mars. The selected data were chosen because of their difference in local time that illuminates two different slices through the interaction region. Although crustal magnetic fields may contribute to the morphology at low altitudes, the magnetic field in the magnetosheath and magnetotail is best described by draping of IMF field lines around the planet. In the next section, we compile data to obtain an average view of the magnetic field morphology rather than this representative view.

4. Compilation of MGS Data

For a more complete view of the magnetic field morphology in the SW interaction with Mars, we compile a global picture from MGS data and investigate how the magnetic field varies as a function of position. First, we investigate the distribution of magnetic field values observed over the course of many spacecraft orbits. Then we average those to produce a single global picture.

We take all the MGS data from within the bow shock for the 746 orbits for which we are able to determine the upstream IMF direction. For each orbit, we remove the data obtained while the spacecraft was directly over a crustal source. This was accomplished by excluding data acquired at an areographic position for which the magnitude of the average magnetic field from the mapping orbits from Connerney *et al.* (2001) ($h \approx 400$ km) is greater than 10 nT. After excluding data that could be contaminated by crustal fields, we further decimate the data volume by computing an average magnetic field vector over each 100 km altitude bin for each orbit. From the elliptical orbits, that leaves 26,777 magnetic field vectors in magnetic coordinates. We then study the magnetic field morphology as a function of position
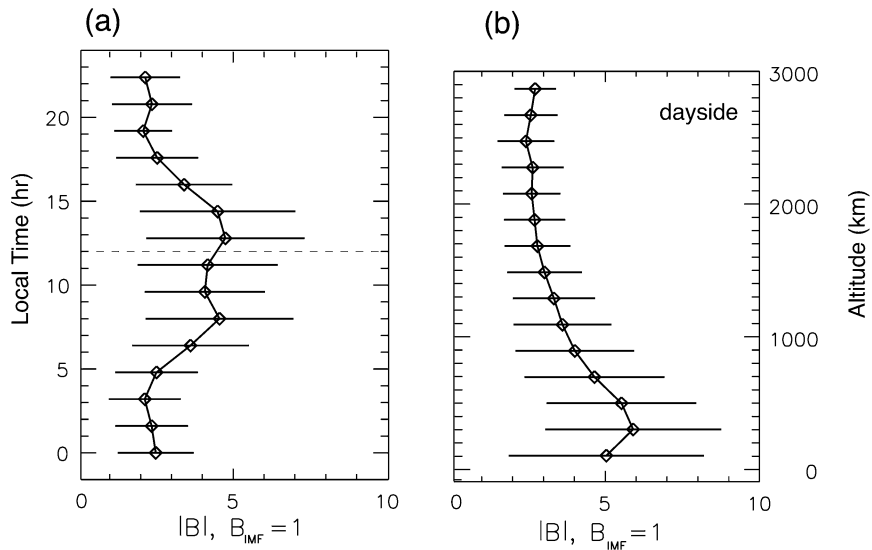
(a) **(b)**

Figure 5. Average (diamond) and 1σ standard deviation (bar) of the magnetic field magnitude are plotted as a function of (a) local time and (b) altitude. The data are from 100 km altitude bins from each MGS elliptical orbit for which the upstream IMF could be determined. Only data from the dayside are included the averages for (b).

by plotting the evolution of the distribution of parameters of these vectors with position.

4.1. MAGNETIC FIELD MAGNITUDE

First, we investigate the evolution of the magnetic field magnitude as a function of position. $|B|$ is expected to peak at the obstacle boundary at low solar zenith angles. Figure 5(a) shows the progression of magnetic field magnitude with local time. In the sector spanning 12:00 ± 3, $\langle |B|/|B_{\mathrm{IMF}}| \rangle$ is highest at 4.0–4.5. Multiplying by the median normalization factor for the upstream IMF, $\langle |B(12:00)| \rangle = 16-18$ nT. These distributions average over all altitudes in the local time bin making the error bars large. The difference with altitude is discussed next. However, note that the magnetic field magnitude distributions are symmetric on the morning and evening sides. Also, note that the standard deviations are smaller on the nightside than on the dayside of Mars showing that the magnetic field magnitude does not vary much on the nightside. The larger error bars on the dayside indicate a wide range of values due to the dramatic pileup of magnetic field in front of the planet.

That pileup can be observed in Figure 5(b), which shows the evolution of $|B|$ with altitude. Figure 5(b) uses only points from the dayside of Mars. $\langle |B| \rangle$ decreases with increasing altitude above 300 km. The magnetic pileup boundary (MPB), defined as the position of steep increase of magnetic field (Vignes *et al.*, 2000), occurs at an altitude between 800–1200 km on the dayside. The magnetic

field remains high in the magnetic pileup region (MPR) which spans the altitude range from the ionosphere to the MPB, generally from 400–1200 km. Figure 5(b) shows that the average magnetic field magnitude drops with increasing altitude even in this region whereas the definition would suggest it would be constant with altitude there. The reason for this is that the magnetic field magnitude at a given altitude drops with solar zenith angle and more low altitude data were obtained near the terminator than at low solar zenith angles.

Brain *et al.* (2003) have already found the MGS average magnetic field magnitude as a function of position in both cylindrical coordinates and in planetocentric coordinates. This investigation confirms their results that the magnetic field magnitude increases with decreasing altitude as the magnetic field piles up in front of the planet. Whereas the Brain *et al.* (2003) study focused on the relative contributions of planetary and SW magnetic fields, this study emphasizes only the SW contribution. Data taken near crustal magnetic fields has been eliminated and the data are presented in the IMF coordinate system.

4.2. INCLINATION ANGLE

One measure of draping of magnetic field around a planet is the average inclination of the magnetic field on the dayside. The inclination angle, I, is defined as the angle the magnetic field makes to the local horizontal, or $I \equiv \text{arc } \sin(B_\rho/|\mathbf{B}|)$, where B_ρ is the radial component of the magnetic field in spherical coordinates (see Figure 1). In a draping configuration, the magnetic field is mostly locally horizontal on the dayside, or $I = 0°$. However, a small radial component does exist simply because the field line is not at a constant altitude as it is wrapped around the planet. Further, the sign of the radial component changes from negative, indicating downward or towards the planet, in the $y < 0$ hemisphere to positive or outward in the $y > 0$ hemisphere.

Uncalibrated MGS data have already been used to show properties of the inclination angle on the dayside of Mars (Crider *et al.*, 2001). They found the average inclination angle was closer to $0°$ within the ionosphere than above it. However, the distribution was much broader within the ionosphere, allowing for the existence of large inclination angles in the martian ionosphere. Now with the calibrated data, we are able to quantify I. Figure 6 is a histogram showing the distribution of I on the dayside of Mars using the same data as in the previous section. The dayside values are divided into two groups depending on the sign of the y coordinate of the observation. The shaded histogram is from points in the western hemisphere where a positive angle is expected. The unshaded histogram is from the points where a negative angle is expected. Both histograms are peaked at an angle offset from zero by $\sim 5°$, indicating a small but finite inclination to magnetic field lines in the draping on the dayside. The distributions are both skewed towards $0°$ which indicates that the magnetic field is rarely nearly-radial and more often nearly-horizontal. Because the orbit by orbit transformation of data to IMF-coordinates is
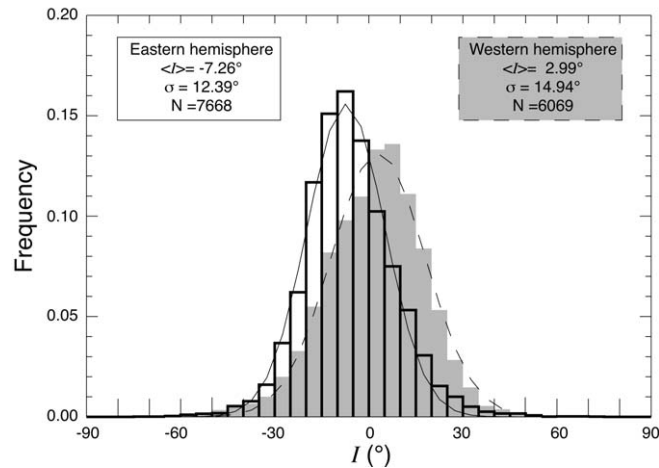
Figure 6. The distribution of observed inclination angles on the dayside of Mars is plotted for points from the eastern (white) and western (gray) hemispheres in magnetic coordinates. Parameters to the superposed Gaussian fit to the distributions are given.

not always accurate, there are some points that are placed in the wrong hemisphere here, especially points close to the $y = 0$ plane. For this reason, we present the evolution of the inclination angle as a function of local time in Figure 7(a).

The local time evolution of the inclination angle is demonstrative of the draping of magnetic field around Mars. Figure 7(a) depicts the constant increase in inclination angle with local time. I passes through zero at local noon and has odd function symmetry about noon. On the dayside, the standard deviations are small, showing that the draping geometry is well defined and the angle of inclination does not vary much with altitude. The distributions broaden on the nightside, however. The standard deviation is large approaching midnight from the a.m. and p.m. sides as would be expected for points in the magnetotail at multiple altitudes.

Although I does not change as much with altitude on the dayside as on the nightside, it has a systematic altitude dependence. We show the explicit evolution with altitude in Figure 7(b). This figure uses data from both the eastern and western hemispheres, but multiplies the inclination angles from the eastern hemisphere by -1 before finding the average and standard deviation for each altitude bin. $\langle I \rangle$ increases monotonically with altitude from $1°$ at 100 km to $13°$ at 1900 km. The standard deviation is minimal from $400-700$ km. This is in agreement with the results of Bertucci *et al.* (2003) that find draping is most well-defined in the magnetic pileup region below the MPB. The higher standard deviation at high altitude reflects the lack of organized draping above the MPB. Note that turbulence exists at these altitudes, but averaging over large spatial bins removes the contribution from waves here. In contrast, below the MPR at ionospheric altitudes the high standard deviation is probably due to ionospheric effects on the magnetic field (Crider *et al.*, 2001). Flux ropes are known to form in the martian ionosphere with random
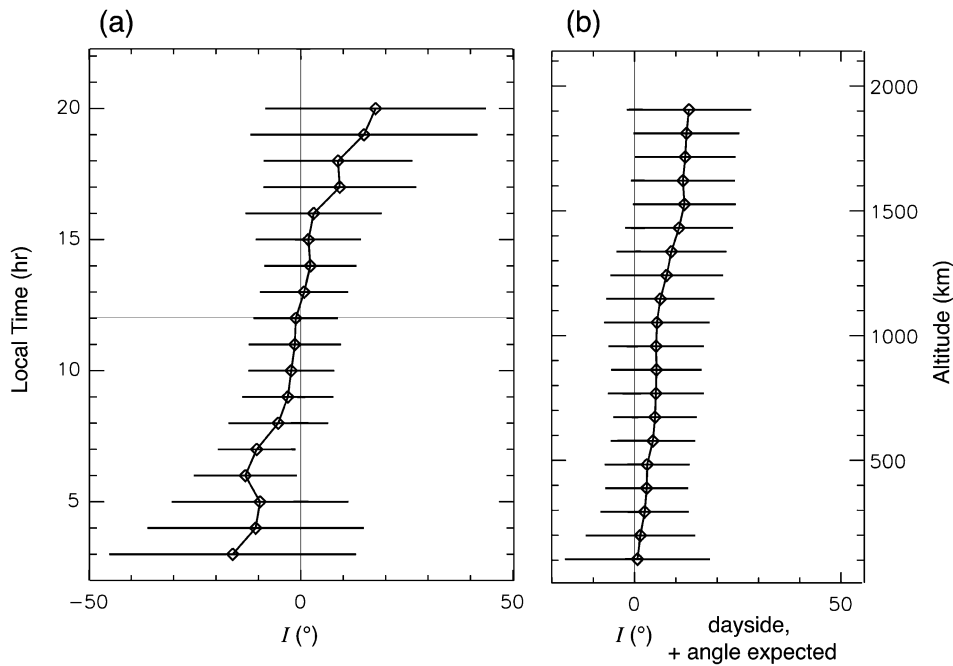
Figure 7. Average (diamond) and 1σ standard deviation (bar) of the angle of inclination of the magnetic field are plotted as a function of (a) local time and (b) altitude. The points used in the altitude plot are taken only from the dayside.

orientation to the local vertical (Vignes *et al.*, 2004). Also, although known crustal sources have been excluded from this data set, magnetic reconnection between IMF and crustal fields can lead to high $|I|$ at locations laterally displaced from the source itself (Brain *et al.*, 2001). Therefore we reaffirm that the ionospheric magnetic field at Mars has an average value that is very close to locally horizontal. However, highly inclined magnetic fields do exist in the ionosphere with high frequency. This fact must be included in ionospheric models of Mars because vertical transport is enabled where inclined magnetic field lines exist.

4.3. FLARE OF THE MAGNETOTAIL

The flaring of magnetic field lines in the magnetotail is another diagnostic parameter of magnetic field draping. The flare angle is defined as the angle the magnetic field makes to the Mars–Sun line, or $\theta_f \equiv \arccos(B_x/|\mathbf{B}|)$ (see Figure 1). The flare angle is related to the width of the magnetotail and influences the shape of plasma boundaries.

As indicated in Figure 1, a hemispheric difference is expected for θ_f in the standard draping picture. The sunward magnetic field in the $-y$ hemisphere leads to a flare angle near $0°$ whereas the tailward field in the $+y$ hemisphere leads to a flare angle near $180°$. Figure 8 shows the distribution of θ_f obtained for the points
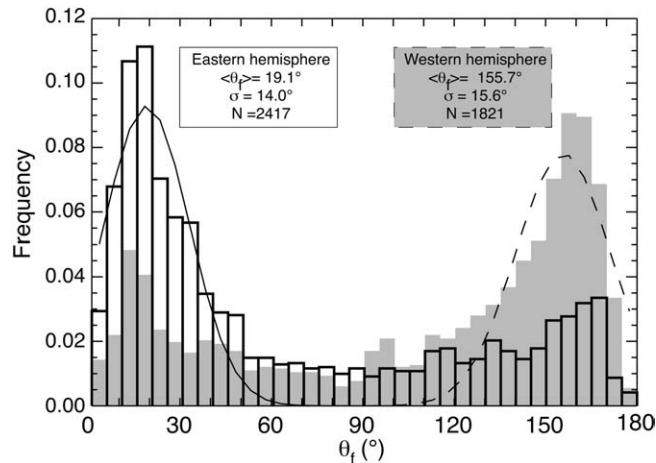
Figure 8. The distribution of observed flare angles on the dayside of Mars is plotted for points from the eastern (white) and western (gray) hemispheres in magnetic coordinates. Parameters to the superposed Gaussian fits to the distributions are given.

with $x < 0$ in the above data set. Two distributions are shown as the data have been separated into y hemispheres. The shaded histogram is the distribution of θ_f from the western hemisphere ($y > 0$ where it is expected that $B_x < 0$) while the unshaded histogram is from the eastern hemisphere. Also plotted are Gaussian fits to the distributions and their parameters. It is important to note that the spacecraft sampling in the tail is not uniform and that there are selection effects inherent in these large spatial groupings. Both distributions are peaked near 21.0° away from the Mars-Sun line and exhibit an excess of data in the same θ_f range as the other hemisphere. These, presumably, correspond to data points that are misplaced by the transformation into IMF coordinates or to places where the neutral sheet is offset from the $y = 0$ plane (Marubashi *et al.*, 1985).

The magnetotail of Mars has already been explored by the Phobos-2 spacecraft and found to have a flare angle of 23° (Luhmann *et al.*, 1991) and 27.2° on average (Zhang *et al.*, 1994; Rosenbauer *et al.*, 1994). The martian magnetotail is known to respond to changes in SW pressure (Verigin *et al.*, 1993; Dubinin *et al.*, 1996). The average angle observed by MGS is close to but slightly smaller than the angle determined from the Phobos-2 data probably due to the difference in spatial coverage of the two spacecraft. Most of the Phobos-2 data come from a distance of 9600 km from the planetary center and from low latitudes. The MGS data was obtained out of the equatorial plane and spans distances from 3700 km to past the Phobos-2 distance. MGS's orbital geometry and helps to fill in a large spatial extent of the tail compared to the region samples by Phobos-2. The spatial distribution of the flare angle is discussed in the following section.

4.4. SPATIAL DISTRIBUTION

Finally, we present global maps of the magnetic field in the martian magnetosheath and magnetotail. To compile global maps of magnetic field morphology, we take cubic bins with sides of length 0.1 R_M in all three Cartesian directions. We average the magnetic field components from each orbital segment that falls within the bin. In doing so, the MGS data is found to cover 5.6% of these bins from the limits $-3\ R_M \leq x \leq 1.6\ R_M$; $|y| \leq -3\ R_M$; $|z| \leq -3\ R_M$. However, by mapping all the data to only one quadrant using the symmetry in Table I, coverage is improved. Still, there are not enough points to present a planar cut through the data set. Instead, we present a projection of points from several z values onto a single $x - y$ half plane in Figure 9. In that projection, the image represents the average morphology of the magnetic field in the martian magnetosheath from multiple z coordinates. The data at positions closer to the Mars–Sun line are from higher $|z|$ coordinates and data at positions far from the Mars–Sun line are from more equatorial locations. The left hand panels in Figure 9 show the average magnetic field morphology from the MGS data. The top panels illustrate the magnitude of the field; the middle panels give the inclination angle; and the bottom panels show the flare angle.

The right hand panels in Figure 9 give the predicted values from the Spreiter and Stahara (1980, 1992) model for the same data coverage as in the data panels. The Spreiter and Stahara model treats the SW as a gasdynamic flow with convected magnetic field. The model was run for $M = 8$. For ease of comparison, the size and color scales are the same for each pair of data and model plots.

The top panels show that the magnitude of the magnetic field is highest in front of the planet. The build up in magnetic field indicates the dominance of magnetic field pressure on the dayside of the planet. $|\mathbf{B}|$ decreases with increasing solar zenith angle. The bulk of the magnetic field pileup begins at the magnetic MPB and it remains high throughout the MPR. The MPR corresponds to the magnetic barrier at Venus (see Zhang *et al.*, 1991) although the magnetic field pileup occurs at higher altitudes at Mars. The GD model falls short of predicting the magnitude of pileup in front of the planet. However, it does a better job if the inner boundary of the model is elevated to the observed MPB position.

The middle panels in Figure 9 show a large green area close to the planet where the magnetic field is primarily horizontal. In contrast, the nightside magnetic field tends to be highly inclined to the local horizontal. This is the magnetic field geometry that is expected in an induced magnetotail (McComas *et al.*, 1986). Note, however, that the highest inclination angles are observed in the martian wake, whereas the gasdynamic model predicts their presence more in the flanks. Nearly radial magnetic fields, such as these, have strong implications for the existence of nightside ionospheric holes at Mars as were observed at Venus (Marubashi *et al.*, 1985). However, the possibility remains that the magnetic field in the martian wake
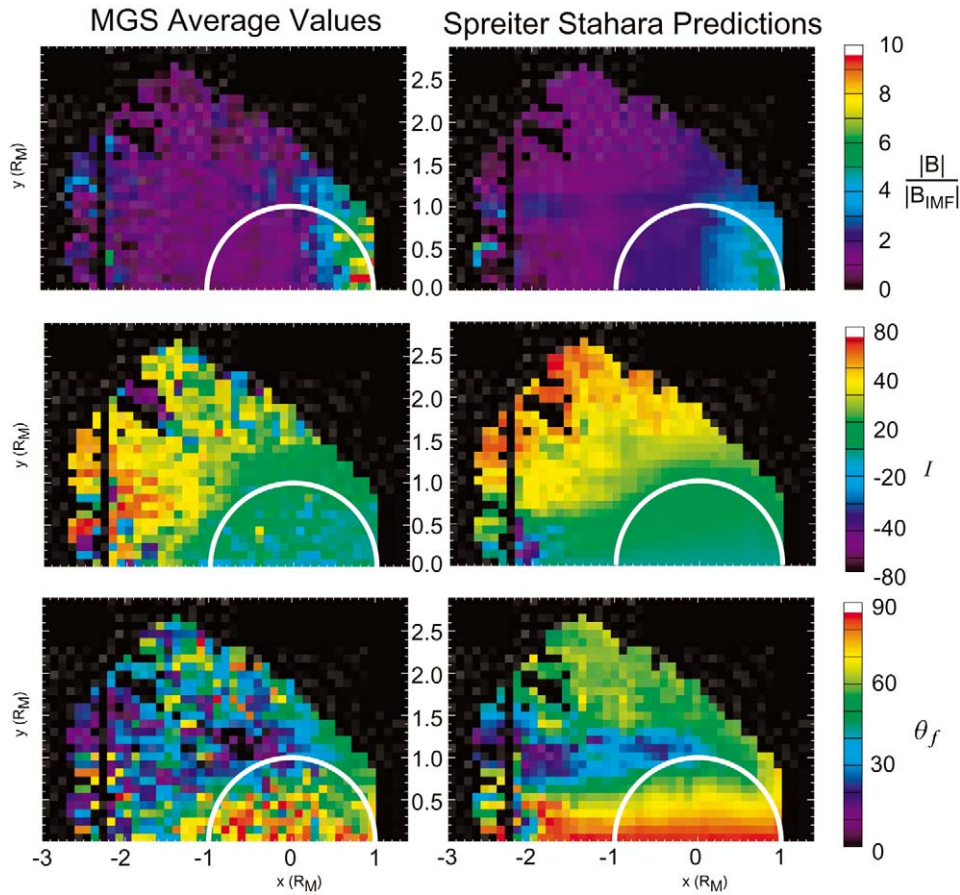
Figure 9. The left-hand panels are the MGS composite of the magnetic field around Mars. The right side shows the GD model predictions using the same coverage as the MGS data. The panels from top to bottom display the magnetic field magnitude, inclination angle, and flare angle.

contains a significant contribution from magnetic flux of planetary origin that leaks out into the tail (Krymskii *et al.*, 2002).

The bottom panels show how the magnetic field rotates from mostly cross-planet ($\theta_f \approx 90°$) close to the Mars–Sun line to a more sunward/tailward orientation ($\theta_f << 90°$) at larger $|y|$. Although only one half plane is shown here, referring to Figure 1 will show how this is the expected geometry as the sign of the B_x component changes at the Mars-Sun line. The gasdynamic model predicts a minimum in the flare angle tailward of the terminator at $y \sim 1 \ R_M$. That minimum also exists in the data; however, it is not as clear. A major difference in the model and measured flare angle appears in the planetary wake, where the high flare angles predicted by the model are not observed. However, this is most likely due to errors in aligning the coordinate systems in the data set as discussed in Section 2. Another difference between the measured and predicted flare angle is that θ_f, especially at

TABLE II

Draping parameters at Mars from MGS MAG data

Parameter	Average	Standard dev.
$|\mathbf{B}|$ (day)	20.7 nT	± 14.7 nT
$|\mathbf{B}|$ (night)	11.6 nT	$\pm\ \ 7.6$ nT
I (day)	5.6°	$\pm 13.6°$
I (night)	12.5°	$\pm 33.6°$
θ_f (night)	21.0°	$\pm 14.8°$

large y, is slightly lower than predicted at all local times. This suggests that the tail is more elongated behind the planet than expected.

The average draping parameters found for certain regions of interest are summarized in Table II. The average dayside magnetic field magnitude at Mars is 20.7 nT. The magnetic field values in this survey are all taken in positions far away from known crustal magnetic sources. Therefore, the magnitude is due primarily to the SW interaction. In the magnetotail, the magnetic field lines flare on average 20° to the x direction. This is slightly lower than predicted by Spreiter and Stahara (1992). The inclination angle of the magnetic field on the dayside is 5.6° on average (where a positive I is expected). Therefore, the dayside magnetic field is predominately locally horizontal. On the nightside, there is a larger radial component to the magnetic field which raises the inclination angle to 12.5° on average with an extremely large scatter about the mean. Again, errors in the mapping and tail asymmetries lead to the large standard deviation and the expectation of negative angles.

5. Conclusion

Compiling data in IMF coordinates from the MGS elliptical orbits shows that on average the magnetic field morphology of the martian magnetosheath is described well by a draping picture. Further, there are no surprises compared to previous work. On the dayside, the magnetic field lines are inclined on average $< 10°$ from the local horizontal. On the nightside, the magnetic field turns to a more radial orientation as the draped IMF produces an induced magnetotail.

We compare both selected data and the compiled data set to model magnetic field predictions from (Spreiter and Stahara, 1992). The GD model typically underestimates the magnitude of magnetic field pileup on the dayside of Mars. It also predicts a broader tail configuration than is observed. For the most part, however, the GD model is an adequate representation of the magnetic field in the SW inter-

action with Mars remote from magnetic crustal sources. It is especially good above the martian MPB.

However, regions of intense crustal magnetization do exist at Mars (Acuña *et al.*, 1998; Connerney *et al.*, 2001; Brain *et al.*, 2003). Now that we have developed a picture of the magnetic field morphology resulting from the SW alone, we will be better able to deconvolve the contributions of the solar wind and planetary magnetic fields in regions where crustal fields play a role. These crustal magnetic fields are the distinguishing feature of the Martian obstacle to the solar wind. Although the MAG/ER instrument has provided much insight into the complex interaction of the solar wind with the martian obstacle, more plasma data are needed to fully unravel the intricacies of the interaction.

Acknowledgement

References

Acuña, M. H., Connerney, J. E. P., Wasilewski, P. *et al.*: 1998, 'Magnetic Field and Plasma Observations at Mars: Initial Results of the Mars Global Surveyor Mission', *Science* **279**(5357), 1676–1680.

Albee, A. L., Arvidson, R. E., Pallucioni, F. and Thorpe, T.: 2001, 'Overview of the Mars Global Surveyor Mission', *J. Geophys. Res.* **106**(E10), 23291–23316.

Alfvén, H.: 1957, 'On the Theory of Comet Tails', *Tellus* **9**, 92–96.

Bertucci, C., Mazelle, C., Crider, D.H. *et al.*: 2003, 'Magnetic Field Draping Enhancement at the Martian Magnetic Pileup Boundary from Mars Global Surveyor Observations', *Geophys. Res. Lett.* **30**(2), 1099, 10.1029/2002GL015713.

Brain, D. A., Bagenal, F., Crider, D. H., Acuña, M. H. and Connerney, J. E.: 2001, *Martian Magnetic Topology: Evaluation of Crustal Magnetization and Solar Wind Interaction Models Using MGS MAG Data*, American Geophysical Union Spring Meeting.

Brain, D. A., Bagenal, F., Acuña, M. H. and Connerney, J. E. P.: 2003, 'Martian Magnetic Morphology: Contributions from the Solar Wind and Crust', *J. Geophys. Res.* **108**(A12), 1424, 10.1029/2002JA009482.

Brecht, S. H.: 1997, 'Hybrid Simulations of the Magnetic Topology of Mars', *J. Geophys Res.* **102**(A3), 4743–4750.

Burlaga, L. F. and King, J. H.: 1979, 'Intense Inter-Planetary Magnetic-Fields Observed by Geocentric Spacecraft During 1963–1975', *J. Geophys. Res.* **84**(NA11), 6633–6640.

Cloutier, P. A., Law, C. C., Crider, D. H. *et al.*: 1999, 'Venus-Like Interaction of the Solar Wind with Mars', *Geophys. Res. Lett.* **26**(17), 2685–2688.

Connerney, J. E. P., Acuña, M. H., Wasilewski, P. J. *et al.*: 2001, 'The Global Magnetic Field of Mars and Implications for Crustal Evolution', *Geophys. Res. Lett.* **28**(21), 4015–4018.

Crider, D. H., Acuña, M. H., Connerney, J. E. P. *et al.*: 2001, 'Magnetic Field Draping around Mars: Mars Global Surveyor Results', *Adv. Space Res.* **27**(11), 1831–1836.

Crider, D. H., Acuña, M. H., Connerney, J. E. P. *et al.*: 2002, 'Observations of the Latitude Dependence of the Location of the Martian Magnetic Pileup Boundary', *Geophys. Res. Lett.* **29**(8), 10.1029/2001 GLO13860.

Dolginov, S. S., Yeroskenko, Y. G., Zhuzgov, L. N.: 1973, 'The Magnetic Field in the Very Close Neighborhood of Mars According to Data from the Mars-2 and 3 Spacecraft', *J. Geophys. Res.* **78**(22), 4779–4786.

Dolginov, S. S.: 1978, 'On the Magnetic-Field of Mars - Mars-5 Evidence', *Geophys. Res. Lett.* **5**(1), 93–95.

Dubinin, E., Sauer, K., Lundin, R. *et al.*: 1996, 'Plasma Characteristics of the Boundary Layer in the Martian Magnetosphere', *J. Geophys. Res.* **101**(A12), 27061–27075.

Kallio, E. J. and Koskinen, H. E. J.: 2000, 'A Semiempirical Magnetosheath Model to Analyze the Solar Wind-Magnetosphere Interaction', *J. Geophys. Res.* **105**(A12), 27469–27479.

Krymskii, A. M., Breus, T. K., Ness, N. F. *et al.*: 2002, 'Structure of the Magnetic Field Fluxes Connected with Crustal Magnetization and Top-Side Ionosphere at Mars', *J. Geophys. Res.* **107** (A9), 1245, doi: 10.1029/2001 JA000239.

Liu, Y., Nagy, A. F., Gombosi, T. I., DeZeeuw, D. L. and Powell, K. G.: 2001, 'The Solar Wind Interaction with Mars: Results of Three-Dimensional Three-Species MHD Studies', *Adv. Space Res.* **27**(11), 1837–1846.

Luhmann, J. G., Russell, C. T., Schwingenschuh, K. and Yeroshenko, Ye.: 1991, 'A comparison of Induced Manetotails of Planetary Bodies: Venus, Mars, and Titan', *J. Geophys. Res.* **96**(A7), 11199–11208.

Marubashi, K., Grebowsky, J. M., Taylor, H. A. *et al.*: 1985, 'Magnetic Field in the Wake of Venus and the Formation of Ionospheric Holes', *J. Geophys. Res.* **90**(NA2), 1385–1398.

Mazelle, C., Bertucci, C., Rème, H. *et al.*: 2002, 'The Magnetic Pileup Boundary at Mars: a Comet-Like Feature in the Interaction of the Planet Atmosphere with the Solar Wind' (in press).

McComas, D. J., Spence, H. E., Russell, C. T. *et al.*: 1986, 'The Average Magnetic-field Draping and Consistent Plasma Properties of the Venus Magnetotail', *J. Geophys. Res.* **91**(A7), 7939–7953.

Mitchell, D. L., Lin, R. P., Mazelle, C. *et al.*: 2001, 'Probing Mars' Crustal Magnetic Field and Ionosphere with the MGS Electron Reflectometer', *J. Geophys. Res.* **106**(E10), 23418–23427.

Ness, N. F., Hundhaus, A. J. and Bame, S. J.: 1971, 'Observations of Interplanetary Medium - VELA 3 and IMP 3, 1965–1967', *J. Geophys. Res.* **76**(28), 6643.

Rosenbauer, H., Verigin, M., Kotova, G., Livi, S. *et al.*: 1994, 'On the Correlation of the Magnetic Field in the Martian Magnetotail to the Solar Wind Parameters', *J. Geophys. Res.* **99**(A9), 17199–17204.

Russell, C. T., Luhmann, J. G., Spreiter, J. R. and Stahara, S. S.: 1984, 'The Magnetic Field of Mars–Implications from Gas-Dynamic Modeling', *J. Geophys. Res.* **89**(NA5), 2997–3003.

Slavin, J. A., Holzer, R. E., Spreiter, J. R., Stahara, S. S. and Chausee, D. S.: 1983, 'Solar-Wind Flow About the Terrestrial Planets 2. Comparison with Gas-Dynamic Theory and Implications Flor Solar-Planetary Interactions', *J. Geophys. Res.* **88**(NA1), 19–35.

Spreiter, J. R. and Stahara, S. S.: 1980, 'A New Predictive Model for Determining Solar Wind-Terrestrial Planet Interactions', *J. Geophys. Res.* **85**(NA12), 6769–6777.

Spreiter, J.R. and Stahara, S. S.: 1992, in J. G. Luhmann, M. Tatrallyay and R. O. Pepin (eds), 'Computer Modeling of the Solar Wind Interaction with Venus and Mars", *Venus and Mars: Atmospheres, Ionospheres, and Solar Wind Interactions*, *Geophysical Monograph* **66**, 345.

Tanaka, T.: 1993, 'Configurations of the Soar-Wind Flow and Magnetic-Field Around the Planets with no Magnetic-Field - Calculation by a New MHD Simulation Scheme', *J. Geophys. Res.* **98**(A10), 17251–17262.

Verigin, M. I., Gringauz, K. I., Kotova, G. A. *et al.*: 1993, 'The Dependence of the Martian Magneto-pause Shape and Bow Shock on Solar Wind Dynamic Pressure According to Phobos 2 TAUS Ion Spectrometer Measurements', *J. Geophys. Res.* **98**(A2), 1303–1309.

Vignes, D., Mazelle, C., Rème, H. *et al.*: 2000, 'The Solar Wind Interaction with Mars: Locations and Shapes of the Bow Shock and the Magnetic Pile-up Boundary from the Observations of the MAG/ER Experiment Onboard Mars Global Surveyor', *Geophys. Res. Lett.* **27**(1), 49–52.

Vignes, D., Acuña, M. H., Connerney, J. E. P., Crider, D. H., Rème, H. and Mazelle, C.: 2004, 'Magnetic Flux Ropes in the Martian Ionosphere: Global Characteristics', *Space Sci. Rev.* **111** (1–2).

Zhang, T. L., Luhmann, J. G. and Russell, C. T.: 1991, 'The Magnetic Barrier at Venus', *J. Geophys. Res.* **96**(A7), 11145–11153.

Zhang, T. L., Schwingenschuh, K., Russell, C. T. *et al.*: 1994, 'The Flaring of the Martian Magnetotail Observed by the Phobos-2 Spacecraft', *Geophys. Res. Lett.* **21**(12), 1121–1124.